

Consistent analysis of the $^{11}\text{B} + ^{120}\text{Sn}$ reaction channels

V. Scarduelli ^{1,*}, L. R. Gasques ¹, L. C. Chamon ¹, V. A. B. Zagatto ², M. A. G. Alvarez ³, and A. Lépine-Szily ¹

¹*Universidade de São Paulo, Instituto de Física, Rua do Matao, 1371, 05508-090, São Paulo, SP, Brazil*

²*Instituto de Física da Universidade Federal Fluminense, 24210-346, Niterói, Rio de Janeiro, Brazil*

³*Departamento de Física Atómica, Molecular y Nuclear, Universidad de Sevilla, Apartado 1065, 41080 Sevilla, Spain*



(Received 25 July 2022; accepted 23 September 2022; published 19 October 2022)

Elastic and inelastic scattering angular distributions have been measured for the $^{11}\text{B} + ^{120}\text{Sn}$ reaction at bombarding energies around the Coulomb barrier: $E_{\text{Lab}} = 31.2, 32.6, 34.7,$ and 37.2 MeV. Additionally, $1p$ stripping and pickup, and 1α stripping yields have been observed in the spectra. Coupled-channel calculations have been performed in the context of the double-folding São Paulo potential. Overall, the theoretical results are in good agreement with the experimental elastic and inelastic scattering angular distributions.

DOI: [10.1103/PhysRevC.106.044606](https://doi.org/10.1103/PhysRevC.106.044606)

I. INTRODUCTION

The investigation of nuclear reactions taking place at energies around the Coulomb barrier can reveal important information about the structure and dynamics of the colliding nuclei. In particular, reactions involving light cluster projectiles are of utmost significance for providing details about the reaction mechanisms at energies around the Coulomb barrier. For instance, the typical low binding energy of the clusters may strongly affect the fusion channel [1]. In recent years, much experimental effort has focused on the study of the main processes of such reactions [2–8]. Measurements of angular distributions of elastic and inelastic scattering, transfer, and fusion excitation functions have been performed for many different systems, which in turn support the developing of new theoretical models [9–12].

In foregoing experimental campaigns performed at the Open Laboratory of Nuclear Physics (LAFN), located at the Institute of Physics of the University of São Paulo, the $^{10}\text{B} + ^{120}\text{Sn}$ reaction has been studied in detail at energies spanning the Coulomb barrier [13–15]. Several processes, such as the excitation of the projectile and target, the $1n$ and $^{3,4}\text{He}$ stripping transfer, the $1p$ and $1d$ pickup transfer, have been experimentally perceived. The production of ^{10}Be has also been observed, which is likely to be related to a two-step transfer process, where a sequential proton pickup followed by a neutron stripping (or vice versa) takes place.

In the present paper, we present new experimental angular distributions for the $^{11}\text{B} + ^{120}\text{Sn}$ reaction measured at energies below and above the Coulomb barrier [$V_B(\text{Lab}) \approx 35$ MeV]. Apart from the elastic channel, yields associated to the excitation of ^{11}B and ^{120}Sn have been observed. The corresponding experimental cross sections are compared to the results of coupled-channel (CC) calculations, which have been performed on the basis of the São Paulo potential (SPP) [16].

In addition, the $1p$ stripping and pickup transfer reactions leading to the formation of ^{10}Be and ^{12}C , respectively, have been identified in the $E - \Delta E$ spectra. Events located in the region of $Z = 3$ have also been detected. Most likely, they are related to the α pickup transfer $^{120}\text{Sn}(^{11}\text{B}, ^7\text{Li})^{124}\text{Te}$ reaction. Unfortunately, it is not possible to experimentally separate the ^{10}B and ^{11}B events lying on the $Z = 5$ band. Therefore, if ^{10}B nuclei coming from the $1n$ transfer reaction are produced, they can not be uniquely identified in the $E - \Delta E$ spectra. Such yields would lie in the same energy region corresponding to the excitation of two ^{11}B states at 4.44 MeV and 5.02 MeV. Besides, at this energy range, there are several ^{120}Sn levels that would also contribute to the $E - \Delta E$ spectra.

The paper is organized as follows. Details of the experimental setup and data analysis are discussed in Sec. II. The experimental results and theoretical CC analyses are presented in Sec. III. A summary of the paper and the main conclusions are presented in Sec. IV.

II. EXPERIMENTAL SETUP AND DATA ANALYSIS

The experiment was conducted at the 8 MV Pelletron accelerator installed at LAFN. Beams of ^{11}B were transported onto a $400 \mu\text{g}/\text{cm}^2$ ^{120}Sn target, placed in the center of the 30B scattering chamber. A thin layer of ^{197}Au with thickness of about $150 \mu\text{g}/\text{cm}^2$ was evaporated over the ^{120}Sn film for normalization purposes. Measurements were carried out at four midtarget beam energies ranging from 31.2–37.2 MeV. The energy loss of the ^{11}B beam in the middle of the ^{120}Sn target is about 300 keV for all incident energies. The beam was produced from $^{\text{nat}}\text{B}$ cathodes mounted in a 32-position MC-SNICS ion source.

The setup was similar to that reported in Refs. [8,15]. Therefore, only a brief description of the experimental arrangement is presented here. Reaction products were detected using two different arrays: SATURN (Silicon Array and Telescopes of USP for Reactions and Nuclear applications) and STAR (Silicon Telescopes Array for low statistics nuclear

*Corresponding author: scarduelli@usp.br

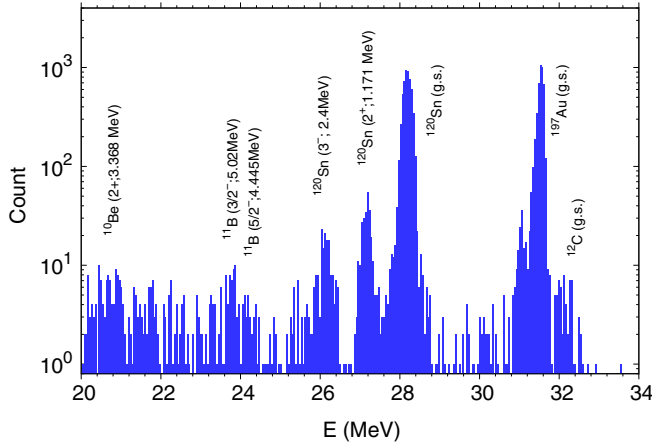


FIG. 1. Single-channel spectrum taken at $E_{\text{Lab}} = 37.2$ MeV and $\theta_{\text{Lab}} = 120^\circ$ with a detector mounted in the SATURN array. Some peaks are identified and labeled in the figure.

Reactions). Single semiconductor silicon surface barrier detectors were placed at SATURN. A typical spectrum taken at $E_{\text{Lab}} = 37.2$ MeV and $\theta_{\text{Lab}} = 120^\circ$ with a single detector is presented in Fig. 1. Several peaks associated to the elastic scattering of the ^{11}B projectile on ^{120}Sn and ^{197}Au targets, and to the inelastic scattering processes and transfer channels have been identified in the figure. For instance, a peak around $E = 32.5$ MeV associated to the proton pickup transfer leading to the ground state (g.s.) of $^{12}\text{C} + ^{119}\text{In}$ can be observed in the spectrum. Also, events related to the proton stripping process is shown in the spectrum at E around 20.8 MeV.

The STAR array was composed by a 50×50 mm 2 $E - \Delta E$ telescope placed at the backward hemisphere, covering an angular region of about 40° . The telescope was formed by a thin $20 \mu\text{m}$ detector segmented into 16 strips coupled to a PAD detector with $1000 \mu\text{m}$. Particle identification was possible based on the energy loss (ΔE) of different species crossing the first detection stage and the residual energy E_r in the second detector of the telescope. A typical two-dimensional ($\Delta E, E_T$) spectrum is presented in Fig. 2, being $E_T = \Delta E + E_r$ the total energy of a given particle. The spectrum was taken $E_{\text{Lab}} = 37.2$ MeV from a strip placed at $\theta_{\text{lab}} = 153.4^\circ$. The lines are the results of energy loss calculations in the ΔE detector as a function of the total energy E_T for the different reaction products [17].

Events corresponding to $Z = 2, 3, 4, 5$, and 6 can be clearly identified in Fig. 2. An inspection in the $Z = 5$ region of the spectrum suggests the formation of ^{10}B , arising from the $1n$ stripping transfer process. However, within the resolution of the $E - \Delta E$ detector, it was impossible to obtain individually the corresponding yields of such channel. To illustrate the situation, a projection in the E_T axis of the $Z = 5$ region is shown in Fig. 3. The peaks located around 30.5 MeV and 25.8 MeV correspond to the elastic scattering of the ^{11}B projectile on ^{197}Au and ^{120}Sn , respectively. The peak around 21.5 MeV in the inset can contain events of the $1n$ stripping transfer process populating states of the residual nuclei in the range of excitation energy from zero (g.s.) to about 1.0 MeV. Additionally, yields coming from the inelastic excitation of

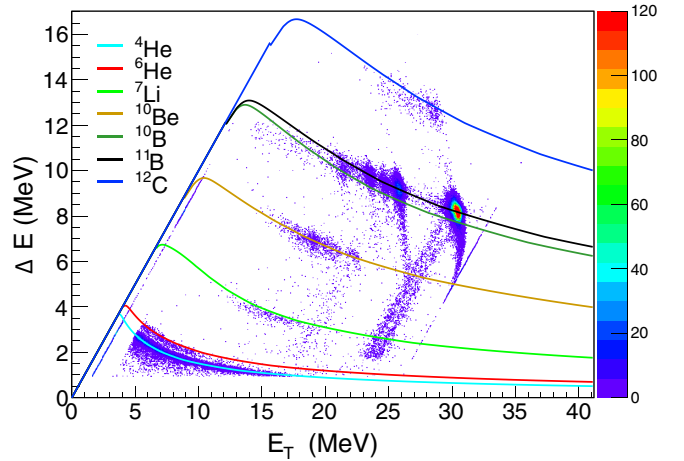


FIG. 2. ($\Delta E, E_T$) spectrum taken with the STAR array at $E_{\text{Lab}} = 37.2$ MeV and $\theta_{\text{Lab}} = 153.4^\circ$. The solid lines correspond to theoretical calculations of energy loss in the ΔE detector for several identified nuclei produced during the collision of ^{11}B on the target composed of ^{120}Sn and ^{197}Au .

the 4.44 MeV ($5/2^-$) and 5.02 MeV ($3/2^-$) ^{11}B states, added to excited states of the ^{120}Sn , would lie in the same energy region of the spectra. Therefore, events of these channels can not be experimentally resolved with the setup adopted in the present measurements. For completeness, the other two peaks in the inset, with centroids around 24.8 MeV and 23.8 MeV, are mainly related to the excitation of the 2^+ (1.17 MeV) and 3^- (2.40 MeV) excited states of the ^{120}Sn target.

III. EXPERIMENTAL AND THEORETICAL RESULTS

Elastic and inelastic scattering angular distributions were experimentally determined using the SATURN and STAR charged particle arrays. CC calculations were performed using

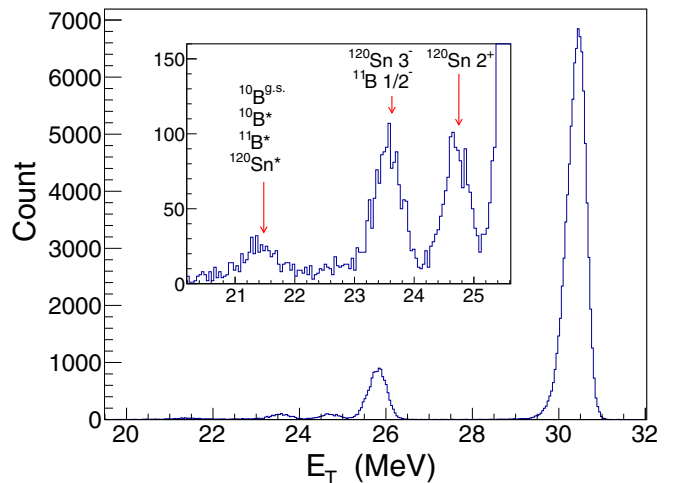


FIG. 3. Projection on the E_T axis of the $Z = 5$ band obtained from the telescope spectrum of Fig. 2. The inset shows a magnification of the spectrum on the Y axis, which corresponds to the number of events acquired along the experiment.

TABLE I. Spin, excitation energies (MeV), transition amplitudes from the g.s. to the excited states ($10^{-3} e^2 b^\lambda$), and deformation lengths (fm), for the inelastic states included in the CC calculations.

| Nucl. | Spin | E^* | λ | $B(E\lambda) \uparrow$ | δ_λ | Ref. |
|-------------------|---------|-------|-----------|------------------------|------------------|------|
| ^{11}B | $1/2^-$ | 2.12 | 2 | 0.26 | 0.44 | [19] |
| ^{11}B | $5/2^-$ | 4.44 | 2 | 2.1 | 1.3 | [19] |
| ^{11}B | $3/2^-$ | 5.02 | 2 | 0.13 | 0.31 | [19] |
| ^{120}Sn | 2^+ | 1.17 | 2 | 230 | 0.68 | [20] |
| ^{120}Sn | 2^+ | 2.10 | 2 | 1.9 | 0.061 | [21] |
| ^{120}Sn | 2^+ | 2.36 | 2 | 3.5 | 0.082 | [21] |
| ^{120}Sn | 3^- | 2.40 | 3 | 115 | 0.74 | [22] |
| ^{120}Sn | 2^+ | 2.42 | 2 | 23 | 0.082 | [21] |
| ^{120}Sn | 2^+ | 2.73 | 2 | 23 | 0.082 | [21] |
| ^{120}Sn | 2^+ | 2.93 | 2 | 7.7 | 0.12 | [21] |
| ^{120}Sn | 2^+ | 3.16 | 2 | 15 | 0.17 | [21] |

the FRESKO code [18]. The SPP was assumed as the bare interaction. For the imaginary part of the optical potential, we have attempted two different approaches: (i) an internal phenomenological Woods-Saxon (WS) parametrization resulting only in flux absorption inside the barrier pocket; (ii) a potential assumed as proportional to the SPP ($W = N_i \times V_{SPP}$). As indicated in Table I, three states related to the excitation of the projectile and eight target states were included in the coupling scheme. We have adjusted the N_i value through data fits within the CC calculations and obtained the best fit with $N_i = 0.20$. Figure 4 presents the elastic scattering angular distributions measured at $E_{Lab} = 31.2, 32.6, 34.7,$ and 37.2 MeV. These energies were determined after considering the energy loss at the middle of the ^{120}Sn target. The black solid and green dashed-dotted curves correspond to no couplings optical model (OM) calculations. While the former was calculated adopting the WS internal imaginary potential ($W_0 = 50$ MeV, $r_{i0} = 0.8$ fm, and $a_i = 0.3$ fm), the latter was evaluated considering $W = 0.2 \times V_{SPP}$. For the lowest energy, both approaches describe

satisfactorily the data within the quoted error bars. As the bombarding energy increases, the cross sections evaluated with the internal WS imaginary potential culminate in a poor description of the data, while the OM results obtained with $N_i = 0.20$ are satisfactory for $E = 32.6$ and 34.7 MeV. For the angular distribution taken at the highest bombarding energy, the description of the data becomes quite poor at $\theta_{c.m.} \gtrsim 140$.

To improve this scenario, a different theoretical approach was attempted, in which CC calculations have been performed on the basis of the SPP. In such calculations, $N_i = 0.20$ for the imaginary potential provides the best data fits. The corresponding results are represented by the red dashed curves in Fig. 4. For the elastic scattering angular distributions measured at 31.2, 32.6, and 34.7 MeV, the OM and CC calculations result in similar outcomes. Both approaches describe adequately the data at the entire angular region. For $E = 37.2$ MeV, the effect of coupling several inelastic states of the projectile and target is clearly important at backward angles.

The cross sections corresponding to the inelastic excitation of the ^{120}Sn ($2^+, 1.171$ MeV) state are shown in Fig. 5 for $E = 34.7$ and 37.2 MeV. The red dashed curve is the result of CC calculations. The remarkable agreement between data and theory can be clearly observed in the figure for the two measured bombarding energies.

Figure 6 shows the inelastic scattering angular distributions for the target 3^- excited state with $E^* = 2.40$ MeV. Although being the uppermost channel, the typical energy resolution of the spectra acquired in the experiment did not allow a separation of other projectile and target excited states from the 3^- state. In fact, the width of the corresponding integrated peak covers an energy range varying from $1.8 \leq E^* \leq 2.8$ MeV. Therefore, as indicated at Table I, the data may contain a contribution of the ^{11}B $1/2^-$ state at $E^* = 2.12$ MeV, apart from few 2^+ states of the ^{120}Sn target at $E^* = 2.10, 2.36, 2.42,$ and 2.73 MeV. The dashed red lines in Fig. 6 are the sum of the cross sections of all such states. Although the strength of the experimental cross section is not perfectly reproduced by the CC calculations, the shape of both theoretical and experimental angular distributions is quite similar. Therefore, the overall agreement between the data and the CC results can be considered satisfactory at the entire angular region for both

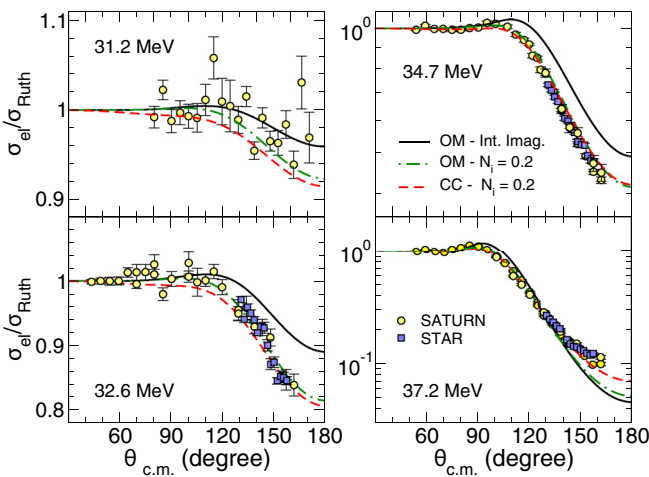


FIG. 4. Elastic scattering angular distributions taken at 31.2, 32.6, 34.7, and 37.2 MeV bombarding energies. The yellow circles and the blue squares correspond to the data obtained with the SATURN and STAR arrays, respectively. Theoretical results are represented by different curves (see text for details).

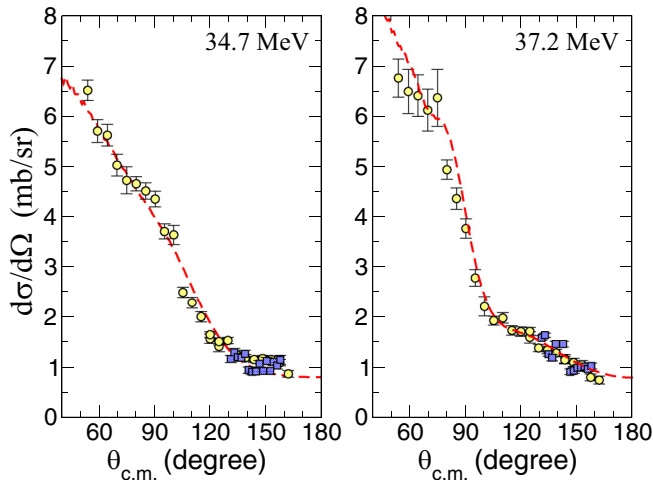


FIG. 5. Inelastic scattering angular distributions for the 2^+ quadrupole ^{120}Sn state with $E^* = 1.17$ MeV. The lines represent the theoretical results of the CC calculations (see text for details).

measurements at $E_{\text{Lab}} = 34.7$ and 37.2 MeV. The quadrupole and octupole transition amplitudes, and the corresponding deformation lengths assumed in the CC calculations, are indicated at Table I. It is worth mentioning that there are several other excited states of the ^{120}Sn target that could contribute to the experimental cross sections plotted in Fig. 6. However, since the transition amplitudes of such states are not known, their couplings have not been included in the CC calculations.

It is worthwhile to compare the outcomes of both $^{10,11}\text{B} + ^{120}\text{Sn}$ reactions, since the most favorable breakup thresholds of the corresponding projectiles are quite different, being 4.46 MeV for ^{10}B ($^6\text{Li} + \alpha$) and 8.66 MeV for ^{11}B ($^7\text{Li} + \alpha$). Notwithstanding, the overall behavior of the both reactions is similar. In a previous work [14], the main channels of the $^{10}\text{B} + ^{120}\text{Sn}$ reaction were well reproduced by CC

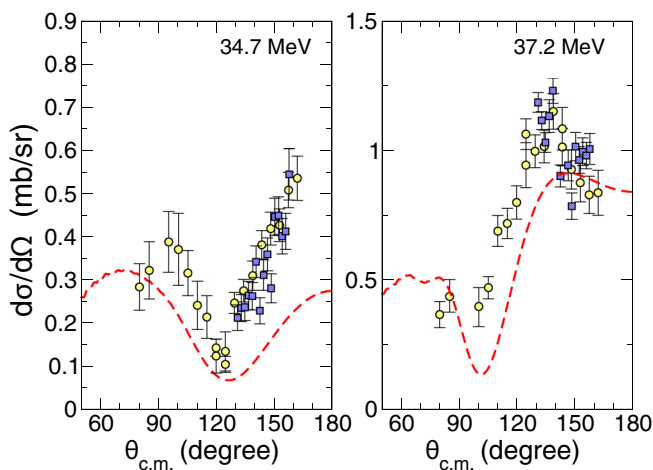


FIG. 6. Same as Fig. 5 for the 3^- octupole ^{120}Sn state with $E^* = 2.40$ MeV. Several other inelastic states from the projectile and target, with excitation energy in the range from $1.8 \leq E^* \leq 2.8$ MeV, can be included in the plotted data. The theoretical lines take into account some of these states, which are indicated in Table I.

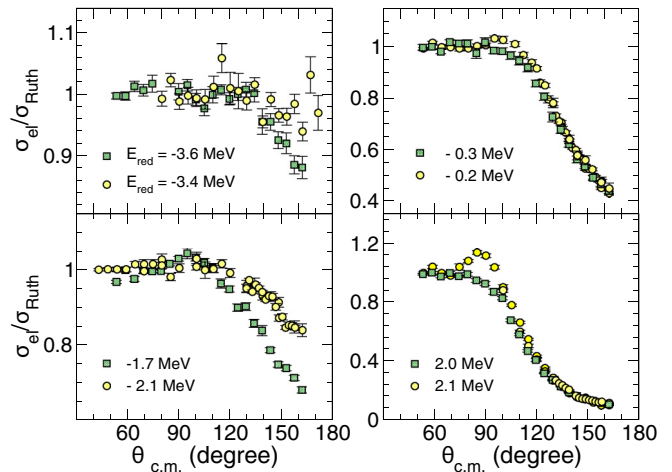


FIG. 7. Experimental elastic scattering angular distributions for the $^{10}\text{B} + ^{120}\text{Sn}$ (green squares) and $^{11}\text{B} + ^{120}\text{Sn}$ (yellow circles) systems. The corresponding E_{red} values are also given in the figure.

calculations in which a normalization factor $N_i = 0.25$ was assumed for the imaginary part of the nuclear interaction. Since the N_i values adopted in the CC calculations for both reactions differ from only 20%, the breakup effect of the ^{10}B seems to have a minor influence on the optical potential. In fact, continuum-discretized coupled-channel calculations support this statement [14]. Nevertheless, as discussed below, there are differences on the elastic scattering angular distributions of both $^{10,11}\text{B} + ^{120}\text{Sn}$ systems that might be related to the breakup channel.

Experimental elastic scattering angular distributions are plotted in Fig. 7 for both $^{10}\text{B} + ^{120}\text{Sn}$ (green squares) and $^{11}\text{B} + ^{120}\text{Sn}$ (yellow circles) reactions. The reduced energy, calculated as $E_{\text{red}} = E_{\text{c.m.}} - V_B$, is given in the figure for each data set. $E_{\text{c.m.}}$ represents the center of mass energy and V_B is the s -wave barrier height (at the center of mass frame) calculated with the SPP. As can be observed in the figure, the angular distributions for the two systems are quite similar at backward angles, for those cases in which the corresponding values of E_{red} are close to each other. However, for the two highest energies the behavior of the cross sections around the Coulomb-nuclear interference region ($\theta_{\text{c.m.}} \approx 90^\circ$) is clearly different for the two systems. In particular, the presence of a pattern typical of rainbow scattering [23] for the $^{11}\text{B} + ^{120}\text{Sn}$ reaction measured at the highest energy is dumped for the $^{10}\text{B} + ^{120}\text{Sn}$ system. This feature could be related to the breakup process since the binding energies of the projectiles are quite different. In fact, similar behavior was reported for $^{9,10,11}\text{Be} + ^{64}\text{Zn}$ [24,25], where the dumping effect is much stronger in comparison with the present case. In that work, the suppression of the Coulomb-nuclear interference peak is associated to a combined effect of Coulomb and nuclear coupling to breakup channels.

At the bombarding energies of $E_{\text{Lab}} = 34.7$ MeV and 37.2 MeV, aside from the identification of yields related to the elastic and inelastic scattering, differential cross sections for the $1p$ stripping, $1p$ pickup, and 1α stripping transfer channels were also experimentally obtained. Table II presents the

TABLE II. Q_{gs} and Q_{opt} values for transfer processes in the $^{11}\text{B} + ^{120}\text{Sn}$ reaction. The Q_{opt} values are provided in MeV units for $E_{Lab} = 34.7$ MeV and 37.2 MeV.

| Exit channel | Q_{gs} (MeV) | 34.7 MeV | 37.2 MeV |
|------------------------------------|----------------|----------|----------|
| $^{12}\text{C} + ^{119}\text{In}$ | 5.269 | 5.594 | 5.997 |
| $^{10}\text{Be} + ^{121}\text{Sb}$ | -5.438 | -5.849 | -6.270 |
| $^7\text{Li} + ^{124}\text{Te}$ | -6.812 | -11.95 | -12.81 |

corresponding g.s. to g.s. Q values (Q_{gs}) and optimum Q values (Q_{opt}) obtained from the matching conditions of the semiclassical trajectory [26]:

$$Q_{opt} = E_{cm} \left(\frac{Z_p^f Z_T^f}{Z_p^i Z_T^i} - 1 \right), \quad (1)$$

where E_{cm} is the center-of-mass energy and $Z_p^f, Z_T^f, Z_p^i, Z_T^i$ are the atomic numbers of the nuclei in the final and initial partitions, respectively. Figures 8(a)–8(c) show the ^{10}Be , ^{12}C , and ^7Li yields (of Fig. 2) projected on the E_T axis, respectively. The arrows in the figure correspond to the approximate position (detected energy of the scattered ejectile) when the final state is the g.s. of both residual nuclei. In the case of Fig. 8(a), there is also an arrow that represents the transition to the final state combining the ^{121}Sb g.s. with the first excited state of ^{10}Be ($2^+ E^* = 3.37$ MeV). There are other arrows in all the panels that represent the detected energy positions that correspond to the Q optimum (Q_{opt}) value for each reaction [26]. Nevertheless, the energy resolution of the STAR telescope makes difficult the experimental determination of cross sections corresponding to individual contributions of a particular state. The experimental angular distributions obtained from the integration of the whole energy region of each spectrum are plotted in Fig. 9. Since the cross sections are associated to a large number of states of the residual nuclei, coupled reaction channel calculations were not performed at the present work.

Finally, one can see the presence of events corresponding to the detection of ^6He at the spectrum of Fig. 2. However, it is clear that part of these nuclei have not enough energy to completely pass through the ΔE detector. Thus, we did not determine the corresponding cross sections in this case.

IV. DISCUSSION AND SUMMARY

Cross sections for elastic, inelastic, and transfer reactions were measured for the $^{11}\text{B} + ^{120}\text{Sn}$ system at bombarding energies around the Coulomb barrier: $E_{Lab} = 31.2, 32.6, 34.7,$ and 37.2 MeV. No couplings OM theoretical calculations for the elastic scattering cross sections were performed adopting two different approaches for the imaginary potential: (i) an internal phenomenological WS parametrization resulting only in flux absorption inside the barrier pocket; (ii) $W = 0.20 \times V_{SPP}$. For the lowest bombarding energy, both OM calculations provide a satisfactory description of the data. However, as the bombarding energy increases, the theoretical cross sections calculated assuming an internal WS imaginary potential result in a poor description of the data, while the OM

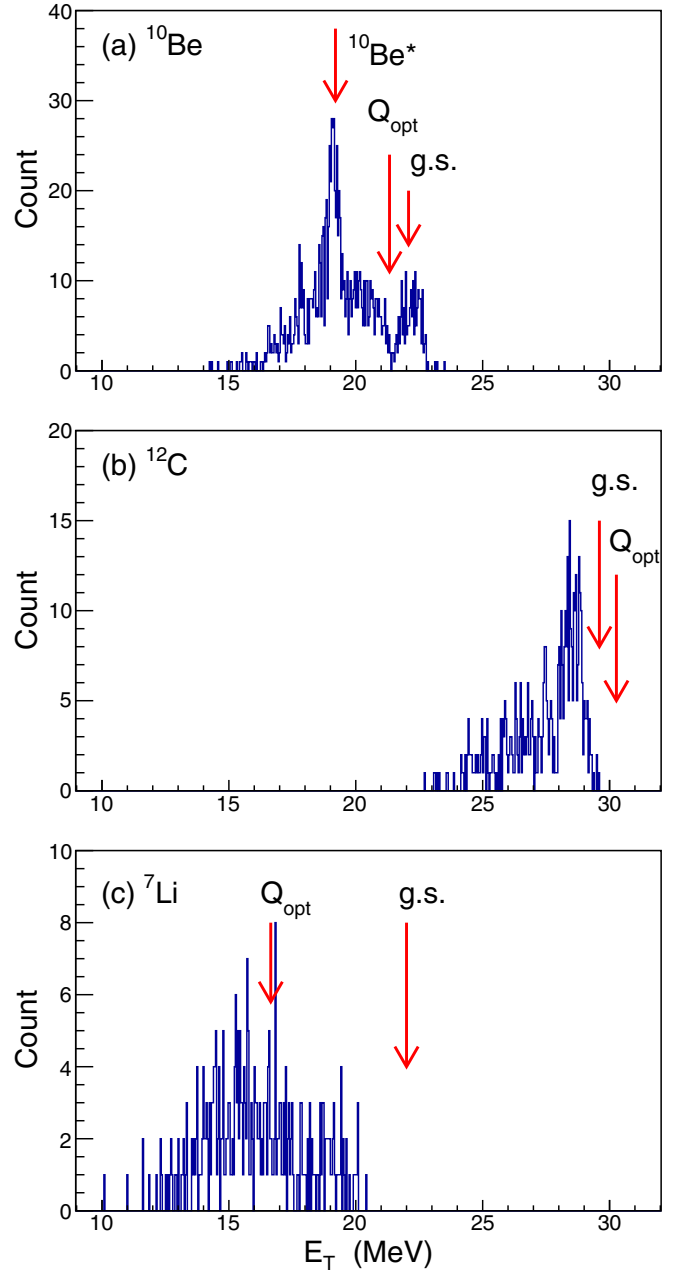


FIG. 8. Yields corresponding to (a) $1p$ stripping, (b) $1p$ pickup, and (c) 1α stripping transfer reactions projected from the telescope spectrum of Fig. 2 on the E_T axis. The arrows in the figure indicate the approximate positions (of the detected energy) that correspond to different Q values for these reactions (see text for details).

results obtained with $N_i = 0.20$ are satisfactory for $E = 32.6$ and 34.7 MeV. In particular, the description of the data becomes insufficient at $\theta_{c.m.} \gtrsim 140$ for the angular distribution measured at the highest bombarding energy ($E = 37.2$ MeV).

An overall satisfactory description of the experimental elastic and inelastic angular distributions was achieved through CC calculations adopting the SPP as the bare interaction. The imaginary potential was assumed to be proportional to the SPP: $W = 0.20 \times V_{SPP}$. In particular, for the backward angular data taken at the highest bombarding energy, the effect

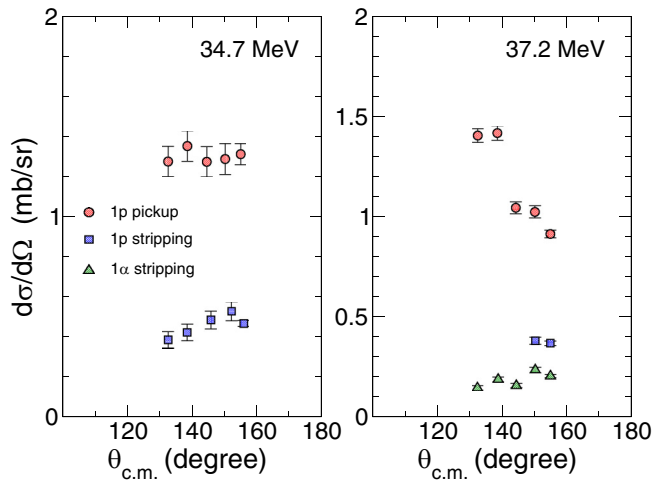


FIG. 9. Transfer angular distributions corresponding to $1p$ stripping (^{10}Be), $1p$ pickup (^{12}C), and 1α stripping (^7Li) reactions.

of coupling several inelastic states of the projectile and target is clearly important.

Besides the differences of the binding energies of the ^{10}B ($4.46\text{ MeV} \rightarrow ^6\text{Li} + \alpha$) and ^{11}B ($8.66\text{ MeV} \rightarrow ^7\text{Li} + \alpha$), the elastic scattering cross sections for both $^{10,11}\text{B} + ^{120}\text{Sn}$ reactions are quite similar at backward angles. Therefore, as already claimed in Ref. [14], it seems that the breakup of the ^{10}B projectile does not affect significantly the elastic channel. On the other hand, a direct comparison of the elastic

scattering cross sections shows a large difference between the data for both systems at the Coulomb-nuclear interference angular region. As plotted in Fig. 7, the cross sections for the $^{11}\text{B} + ^{120}\text{Sn}$ reaction measured at $E_{\text{Lab}} = 34.7$ and 37.2 MeV present a typical pattern of rainbow scattering around $\theta_{\text{c.m.}} \approx 90^\circ$, while the ^{10}B scattering shows a reduction of the elastic cross section at the same angular region. This could be associated to couplings to breakup channels.

ACKNOWLEDGMENTS

This work was partially supported by Fundação de Amparo à Pesquisa do Estado de São Paulo (FAPESP) Proc. No 2019/05769-7 and No, 2019/07767-1, Fundação de Amparo à Pesquisa do Estado do Rio de Janeiro (FAPERJ) Proc. No E-26/211.386/2021(269750), and Conselho Nacional de Desenvolvimento Científico e Tecnológico (CNPq) Proc. No 304056/2019-7, No. 302160/2018-3, No. 301842/2019-1, No, 304750/2021-2, No. 406332/2018-5, and project INCT-FNA Proc. No 464898/2014-5. M.A.G.A. is supported by the Grant Group FQM-160 funded by the Consejería de Economía, Conocimiento, Empresas y Universidad from the Junta de Andalucía; the Spanish Ministerio de Ciencias, Educación e Innovación under Project No. PGC2018-096994-B-C21; and the Project No. P20-01247, within the Andalusian Plan for Research, Development and Innovation (PAIDI), funded by the Consejería de Economía, Conocimiento, Empresas y Universidad from the Junta de Andalucía with funds from the European Regional Development Fund “ERDF A way of making Europe”.

- [1] M. Dasgupta *et al.*, *Phys. Rev. C* **70**, 024606 (2004).
- [2] L. R. Gasques, M. Dasgupta, D. J. Hinde, T. Peatey, A. Diaz-Torres, and J. O. Newton, *Phys. Rev. C* **74**, 064615 (2006).
- [3] J. C. Zamora *et al.*, *Phys. Rev. C* **84**, 034611 (2011).
- [4] S. Kalkal, E. C. Simpson, D. H. Luong, K. J. Cook, M. Dasgupta, D. J. Hinde, I. P. Carter, D. Y. Jeung, G. Mohanto, C. S. Palshetkar, E. Prasad *et al.*, *Phys. Rev. C* **93**, 044605 (2016).
- [5] V. A. B. Zagatto, J. Lubian, L. R. Gasques, M. A. G. Alvarez, L. C. Chamon, J. R. B. Oliveira, J. A. Alcantara-Nunez, N. H. Medina, V. Scarduelli, A. Freitas, I. Padron, E. S. Rossi, and J. M. B. Shorto, *Phys. Rev. C* **95**, 064614 (2017).
- [6] A. Kundu, S. Santra, A. Pal, D. Chattopadhyay, R. Tripathi, B. J. Roy, T. N. Nag, B. K. Nayak, A. Saxena, and S. Kailas, *Phys. Rev. C* **95**, 034615 (2017).
- [7] M. Aversa *et al.*, *Phys. Rev. C* **101**, 044601 (2020).
- [8] L. R. Gasques *et al.*, *Phys. Rev. C* **101**, 044604 (2020).
- [9] A. Diaz-Torres, D. J. Hinde, J. A. Tostevin, M. Dasgupta, and L. R. Gasques, *Phys. Rev. Lett.* **98**, 152701 (2007).
- [10] L. F. Canto, P. R. S. Gomes, R. Donangelo, J. Lubian, and M. S. Hussein, *Phys. Rep.* **596**, 1 (2015).
- [11] J. Rangel, M. R. Cortes, J. Lubian, L. F. Canto *et al.*, *Phys. Lett. B* **803**, 135337 (2020).
- [12] M. R. Cortes, J. Rangel, J. L. Ferreira, J. Lubian, and L. F. Canto, *Phys. Rev. C* **102**, 064628 (2020).
- [13] L. R. Gasques *et al.*, *Phys. Rev. C* **97**, 034629 (2018).
- [14] M. A. G. Alvarez *et al.*, *Phys. Rev. C* **98**, 024621 (2018).
- [15] L. R. Gasques *et al.*, *Phys. Rev. C* **103**, 034616 (2021).
- [16] L. C. Chamon *et al.*, *Phys. Rev. C* **66**, 014610 (2002).
- [17] V. Scarduelli, L. R. Gasques, L. C. Chamon, and A. Lépine-Szilgyi, *Eur. Phys. J. A* **56**, 24 (2020).
- [18] I. J. Thompson, *Comput. Phys. Rep.* **7**, 167 (1988).
- [19] T. Kawabata *et al.*, *Nucl. Phys. A* **788**, 301 (2007).
- [20] S. Raman, C. W. Nestor Jr., and P. Tikkanen, *At. Data Nucl. Data Tables* **78**, 1 (2001).
- [21] <https://www.nndc.bnl.gov/ensdf/>, Evaluated Nuclear Structure Data File
- [22] T. Kibédi and R. H. Spear, *At. Data Nucl. Data Tables* **80**, 35 (2002).
- [23] S. Fricke *et al.*, *Nucl. Phys. A* **500**, 399 (1989).
- [24] A. Di Pietro, G. Randisi, V. Scuderi, L. Acosta, F. Amorini, M. J. G. Borge, P. Figuera, M. Fisichella, L. M. Fraile, J. Gómez-Camacho, H. Jeppesen, M. Lattuada, I. Martel, M. Milin, A. Musumarra, M. Papa, M. G. Pellegriti, F. Perez-Bernal, R. Raabe, F. Rizzo *et al.*, *Phys. Rev. Lett.* **105**, 022701 (2010).
- [25] A. DiPietro, V. Scuderi, A. M. Moro, L. Acosta, F. Amorini, M. J. G. Borge, P. Figuera, M. Fisichella, L. M. Fraile, J. Gomez-Camacho, H. Jeppesen, M. Lattuada, I. Martel, M. Milin, A. Musumarra, M. Papa, M. G. Pellegriti, F. Perez-Bernal, R. Raabe, G. Randisi, F. Rizzo, G. Scalia, O. Tengblad, D. Torresi, A. M. Vidal, D. Voulot, F. Wenander, and M. Zadro, *Phys. Rev. C* **85**, 054607 (2012).
- [26] R. Broglia and A. Winther, *Heavy Ion Reactions: Lecture Notes the Elementary Processes*, Frontiers in Physics Vol. 84 (Addison-Wesley, Redwood City, CA, 1991).